Research in Astronomy and Astrophysics, 23:065005 (9pp), 2023 June https://doi.org/10.1088/1674-4527/accbb1

Relation between Mass and Radius of Exoplanets Distinguished by their Density

Alberto S. Betzler[1] and José G. V. Miranda[2]
[1] Centro de Ciência e Tecnologia em Energia e Sustentabilidade, Universidade Federal do Recôncavo da Bahia, Feira de Santana, Bahia, 44.085-132, Brazil
betzler@ufrb.edu.br
[2] Instituto de Fisica, Universidade Federal da Bahia, Salvador, Bahia, 40.170-115, Brazil
Received 2022 December 28; revised 2023 March 22; accepted 2023 April 7; published 2023 May 10

Abstract

The formation of the solar system has been studied since the 18th century and received a boost in 1995 with the discovery of the first exoplanet, 51 Pegasi b. The investigations increased the number of confirmed planets to about 5400 to date. The possible internal structure and composition of these planets can be inferred from the relationship between planet mass and radius, *M–R*. We have analyzed the *M–R* relation of a selected sample of iron-rock and ice-gas planets using a fractal approach to their densities. The application of fractal theory is particularly useful to define the physical meaning of the proportionality constant and the exponent in an empirical *M–R* power law in exoplanets, but this does not necessarily mean that they have an internal fractal structure. The *M–R* relations based on this sample are $M = (1.46 \pm 0.08)R^{2.6\pm0.2}$ for the rocky population ($3.6 \leqslant \rho \leqslant 14.3$ g cm^{-3}), with $1.5 \leqslant M \leqslant 39$ $M_\oplus$, and $M = (0.27 \pm 0.04)R^{2.7\pm0.2}$ for ice-gas planets ($0.3 \leqslant \rho \leqslant 2.1$ g cm^{-3}) with $5.1 \leqslant M \leqslant 639$ $M_\oplus$ (or $\simeq 2\,M_J$) and orbital periods greater than 10 days. Both *M–R* relations have in their density range a great predictive power for the determination of the mass of exoplanets and even for the largest icy moons of the solar system. The average fractal dimension of these planets is $D = 2.6 \pm 0.1$, indicating that these objects likely have a similar degree of heterogeneity in their densities and a nearly similar composition in each sample. The *M–R* diagram shows a "gap" between ice-gas and iron-rock planets. This gap is a direct consequence of the density range of these two samples. We empirically propose an upper mass limit of about 100 $M_\oplus$, so that an *M–R* relation for ice-gas planets in a narrow density range is defined by $M \propto R^3$.

Key words: planets and satellites: formation – planets and satellites: terrestrial planets – planets and satellites: gaseous planets

1. Introduction

The formation of planets is modeled by the standard model, which proposes the successive accumulation of gas and dust by the combination of gravitational force and successive collisions, which would lead to the formation of planetesimals and these to planets. In this model, the Keplerian orbits of these objects, as the dust condenses into small meteoroids, would result in collisions at relative velocities of probably a few kilometers per second. Such collisions would cause the fragments to reach velocities exceeding the escape velocity of the system. The formation of bodies with large mass/dimension would not be expected in such a situation. Experiments with growth models (Peak 1992; Katyal et al. 2014) suggested that Diffusion-Limited Aggregation (DLA) could mediate growth at some early stages of grain coagulation. This formation process would involve fragile dust balls with fractal filament structure described by the dynamics of the DLA model instead of compact dust grains. The orbits of these fractal dust balls are slowed by friction with the gas cloud, ensuring that the relative velocity of the interaction is much smaller than the Keplerian orbital velocity. Consequently, these fractal strands can collide and stick together, forming larger strands. This low-velocity coagulation process (<10 m s^{-1}) can manifest itself in the "dust trap" phenomenon (Li 2020), its occurrence having been observed in the Oph IRS 48 system (Bruderer et al. 2014). Computer simulations suggest that objects with masses $>1\,M_\oplus$ can grow into a dust trap (Owen & Kollmeier 2017) on short timescales (10^4–10^5 yr).

Planets are many orders of magnitude more massive than dusty aggregates and so massive that their self-gravity can overcome material forces and achieve hydrostatic equilibrium and a nearly spherical shape, meaning there is little porosity inside. However, there are numerous studies showing that even individual objects with no apparent fractal structure can be described by fractals when analyzed in groups: The surface of the Earth and many solar system bodies can be adequately represented by fractals (e.g., Landais et al. 2019; Pardo-Igúzquiza & Dowd 2022), an assumption that also holds for the distribution of young open star clusters in the solar neighborhood (de La Fuente Marcos & de La Fuente Marcos 2006) and even for large-scale structures in the universe (Teles et al. 2021). The distribution of solar system planetary mass and radius can be approximated by a Cantor multifractal (Siekman 2001), which reflects the likely aggregation of primordial fractal dust clusters in the Sun's protoplanetary disk. These planets can be described by a power law *M–R* mass–radius relationship. Therefore, the *M–R* relation could also be defined by a fractal approach to planet density, which does not necessarily mean that they have an internal fractal structure.

In this paper we show that the application of fractal theory is particularly useful in defining the physical meaning of the constant of proportionality and exponent in an empirical *M–R* power law in exoplanets. The fractal approach to the *M–R* relation in exoplanets allows the identification of planets with similar or nearly similar composition by estimating the degree of heterogeneity in their densities. We also discuss the importance of setting appropriate physical constraints, especially density, when selecting exoplanets for establishing an *M–R* relation.

2. The Model

Analytical expressions for the *M–R* relation for planetary bodies can be derived from equations of state (EoSs) that describe density ρ as a function of pressure P, temperature and composition. EoSs for various solid and liquid materials can be described by a simple polytropic equation

$$P = K\rho^{\frac{n+1}{n}}, \tag{1}$$

where n is the polytropic index and K is a constant. The temperature and phase changes are neglected, since they have only a small influence on the mass–radius ratio. The mass and radius of the corresponding polytrope are obtained by integrating the hydrostatic and Poisson's equations (see Queloz et al. 2007). The mass–radius relationship is such that

$$R \propto M^{\frac{1-n}{3-n}}. \tag{2}$$

The relationship between mass and radius behaves differently depending on the value of the polytropic index. For non-compressible materials, $n = 0$ and

$$R \propto M^{1/3} \text{ or } M \propto R^3. \tag{3}$$

This general relation is a good approximation for terrestrial planets and gas planets of H and He with a mass of $\lesssim 30\, M_\oplus$, since the H and He material is not yet strongly compressed under these conditions. Planets around the mass of Jupiter (or 318 $M_\oplus$) have $n \sim 1$, which effectively corresponds to a maximum in the polytropic mass–radius (Equation (2)). The radius begins to decrease with increasing mass above 4 M_J (or $\sim$1300 $M_\oplus$), and an object with 10 M_J (3200 $M_\oplus$) has $n \approx 1.3$ in most of its interior. This would mean $R \propto M^{-0.18}$. Objects whose internal pressure is dominated by non-relativistic degenerate electrons, which formally applies only to white dwarfs, are those where $n = 1.5$ and $R \propto M^{-1/3}$.

Commonly used EoSs to characterize planetary interiors are 3rd order Birch–Murnaghan, Mie–Grüneisen–Debye (Jackson 1998; Sotin et al. 2007) and Generalized Rydberg (Wagner et al. 2012). These EoSs differ in whether or not they take temperature dependence into account. Baumeister et al. (2018) performed an extensive parameter study to model the internal structure of a large number of subneptunian exoplanets of different compositions, ranging from super-Earths consisting only of a metallic core and silicate mantle to subneptunes with ice and gas layers. They found that for the rocky interior of an exoplanet, the choice of EoS has little effect on characterizing the planet's internal structure, and that for Earth-like planets, a simple isothermal EoS such as the third-order isothermal Birch–Murnaghan EoS is sufficient to accurately model their interiors.

Seager et al. (2007) modeled solid exoplanets using the isothermal Vinet and Birch–Murnagh EoS (Vinet et al. 1986), which is a modification of the Birch–Murnaghan EoS

$$\rho = \rho_0 + cP^k, \tag{4}$$

where c and k are constants that depend on the chemical composition of the planet, and ρ_0 is its density at $P = 0$. This last equation is a good approximation to the more complex EoS for small terrestrial planets. It is therefore clear that Equation (4) has the same form as the inverse function of Equation (1), with the addition of the constant ρ_0. This constant is required for solid planets because non-gaseous matter is nearly incompressible at low pressures. Equation (4) accurately models the internal density, but for smaller planets with lower central pressure ($P < 10^{12}$ Pa), the density remains essentially the same throughout the planet (Tucker & Nepsky 2011).

The *M–R* relationship for exoplanets can also be interpreted with a fractal approach.

Fractal theory attempts to generalize the scaling patterns in the formation of complex systems in nature. These patterns can exhibit a variety of structuring mechanisms and formation dynamics, as in the classic example of Romanesco broccoli, which exhibits self-similar fractal patterns in its formation (Mandelbrot 1982); in the particle size distribution in the granulometry of a soil (Miranda et al. 2006), where fractal theory is expressed in terms of the relationship accumulated volume of particles versus radius; in the scaling of the volume of particles versus radius; in the scaling of the radius; in the scaling of the semivariance of rough surfaces (Vázquez et al. 2005); in the porous system of a solid, where the fractal dimension is estimated from the relation between cumulative pore volume and intrusion pressure (Paz-González et al. 2010); in the fracture of solid objects from the relation between tensile force and size of the object (Carpinteri & Ferro 1994); and more recently, Cheng (2017) proposed a new approach to characterize systems whose fractality is determined from the property of density.

The fractal behavior of density on a set of objects is particularly useful in characterizing a system whose elements are homogeneously shaped but whose masses may vary over a range of different magnitudes. The authors propose the following definition of fractal density ρ_D,

$$\rho_D = \lim_{V \to 0} \frac{M}{V^{D/3}}, \tag{5}$$

where V and M are the volume and mass, respectively, of the object of the system and D is the fractal dimension. Fractal density is a statistical property defined by Cheng (2017) as a generalized density that, together with the fractal dimension, characterizes the density distribution pattern of a heterogeneous system. In this approach, the values of the fractal dimension represent the heterogeneity of densities in the set and define planets with nearly similar or similar internal composition. More precisely, for $D = 3$ the density is approximately constant for the scales of the system, for $D < 3$ implies a sample with a mixture of different compositions/densities, and the volume increases more slowly than the mass for $D > 3$. It is important to note that the fractal dimension in this approach characterizes not the internal structure but the diversity in the composition/density of a group of planets.

Following Chen & Cheng (2017), the density definition ($\rho = \lim_{V\to 0}\frac{M}{V}$) can be rewritten in a more general way by comparing it to Equation (5),

$$\rho = \rho_D r_i^{D-E}, \tag{6}$$

where ρ is the density, r is its scale factor (radius or diameter), and E is the immersion dimension from which the density was calculated. In the case of $D = E$, we obtain the case of linear formation dynamics where the fractal density coincides with the density. For the case of a system consisting of a set of approximately spherical objects, we can apply Equation (6) to the definition of the density of the ith element,

$$\rho_i = \frac{M_i}{\frac{4}{3}\pi r_i^3}, \tag{7}$$

that for $E = 3$ and considering that the fractal density is the same for all objects within the group, the mass–radius relation can be rewritten in the form

$$M_i = \rho_D \frac{4}{3}\pi R_i^D. \tag{8}$$

This is a generalization of the mass–radius relation for a group of objects with irregular densities. For planets with similar composition i.e., $D = 3$, ρ_D is equal to the density.

To better understand the implications of Equation (8), we illustrate in Figure 1 some hypothetical distributions of mass and radius for different configurations: same fractal dimension and different fractal densities (black and red curves respectively) and same fractal density with different fractal dimension values (red and blue curves respectively).

A possible planetary composition could be derived by comparing the mass–radius relation for exoplanets and a series of models derived from the EoSs for different internal constitutions. Another way to classify planets is by average density. A rough proposal based on the planets of the solar system suggests that high density objects are composed of rock and iron, intermediate density objects contain a significant fraction of water ice (Showman & Malhotra 1999), while low density objects have a significant fraction of their volume composed of H and He (Guillot 1999). We applied this last method to classify the planets in our sample, also taking into account the fact that an object with a given composition can have a range of densities depending on its mass, as shown for example in Figure 2 of Lissauer et al. (2014).

3. Sample Selection

Data on extrasolar systems for this article are from The Extrasolar Encyclopaedia,[3] published 2022 March 25. Our original sample included 1006 planets with known masses and radii and their respective errors, and consisted of objects confirmed by primary transits and direct imaging methods (Figure 2(a)). We selected planets discovered by these two methods to minimize systematic errors in the observations, as the different detection methods have different accuracies in determining planet masses and/or radii, allowing for the composition of a homogeneous sample; 94.1% of this initial sample are planets discovered by primary transits, and 74% of these planet masses were determined by the radial velocity method. Photometric transit light curves provide estimates of planetary radii and orbital inclinations. The drop in the transit light curve is related to the relationship between planetary and stellar radii. Stellar radii can be estimated using methods such as isochrones and spectral energy distribution fitting that have a small discrepancy (∼6%) with each other (Duck et al. 2022). The radial velocity method combined with the orbital inclination provided by the transit allows the planetary mass to be determined. The combination of the radius of the transiting object and its mass can be used to determine the density of a planet (Drake & Cook 2004).

It is necessary to apply a series of cut-offs in this sample to constrain the influence of the M–R relationship of exoplanets on the density/composition so that it can be interpreted using Equation (8) derived from fractal theory.

Uncertainties in the determination of the mass and radius of the planets vary in the initial sample. These parameters show an asymmetric distribution of the relative uncertainties of mass and radii with medians of 14.3% and 4.8%, respectively. These medians defined the threshold for the uncertainties in the sample in a procedure similar to that used by Otegi et al. (2020). The sample was reduced to 296 planets using this

[3] http://exoplanet.eu/

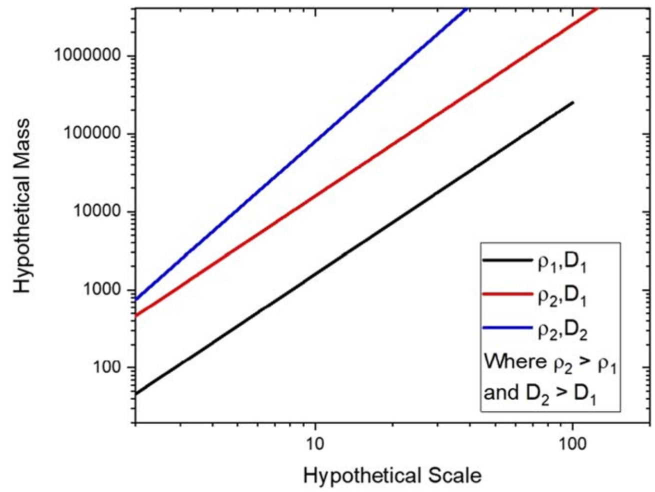

Figure 1. Effect of different configurations of fractal density and dimension in the *M*–*R* relation for hypothetical objects following Equation (8).

procedure (Figure 2(b)). This residual sample has a wide range of masses, from 1.5 to about 19,000 Earth masses, suggesting objects of various types, such as super-Earths, mini-neptunes, gas giants and brown dwarf candidates. We have excluded objects with masses greater than 4 M_J (or $\sim$1300 $M_\oplus$) because their radius begins to decrease according to the polytropic model based on Equation (1). These remaining objects were divided into two classes according to their density: ice-gas ($0.3 \leqslant \rho \leqslant 2.1$ g cm^{-3}) and rock-iron ($3.6 \leqslant \rho \leqslant 14.3$ g cm^{-3}) planets, following the classification scheme of Odrzywolek & Rafelski (2018). The materials of each class may correspond to the possible internal constituents of gas giants and rocky planets and include 23 and 158 objects, respectively (Figure 2(c)). The gas planets have a large dispersion in their radii of about 70 Earth masses. This scatter is high even when a median relative uncertainty of 16.2% for the density is taken into account. An analysis of this sample revealed the presence of 125 hot Jupiters, gas giants with masses greater than or equal to 0.25 Jupiter masses and orbital periods shorter than 10 days (Dawson & Johnson 2018), which are subject to strong stellar irradiation. Planets composed of low-mass H-He tend to have larger radii than predicted by polytropic solutions for non-irradiated planets (Queloz et al. 2007). These hot Jupiter candidates were excluded from the gas giant sample, which was eventually reduced to 33 objects (Figure 2(d)). Iron-rock planets have masses between 1.5 and 39 Earth masses (Table 1) and are considered low-mass planets by the definition of Hatzes & Rauer (2015) and include the candidate remnant core of a giant planet TOI-849 b (see Armstrong et al. 2020) as an upper limit. The final sample of ice-gas planets has masses ranging from 5.1 to 639 Earth masses and ranges from low-mass to low-mass giant planets (Table 2).

The distribution of spectral types of the parent star is different for the gas and rocky planets. There are 35.3% and 15.0% of M stars with rocky and gaseous planets, respectively. This fact could be a consequence of the detection efficiency of different surveys and selection biases (Mulders 2018). The lower stellar mass of M-type stars compared to more Sun-like stars with spectral types F, G and K facilitates the detection of less massive planets with radial velocity techniques (e.g., Endl et al. 2003). Similarly, the small size of M dwarfs compared to Sun-like stars leads to deeper transits for a planet of the same size (Dressing & Charbonneau 2015).

The distributions of metallicity of the parent stars of ice-gas and iron-rock planets are Gaussian, with means of 0.09 and 0.05 and large standard deviations ($\sigma = 0.18$ and 0.21) respectively. The mean [Fe/H] values suggest that gas giant planets may be associated with stars with higher metallicity, a result previously reported in Thorngren et al. (2016). The t-test suggests that the distributions are similar (p-value = 0.24), assuming a confidence level of $\alpha = 0.05$. The Spearman correlation test indicates that the correlation between metallicity and planet mass in both planet samples cannot be considered statistically significant ($\rho = 0.27$ and 0.36). These statistical analyses indicate that there is no clear relationship between the formation of ice-gas or iron-rock planets and the metallicity of the parent star in the sample considered here. Of course, this condition could be a consequence of the selection effect in our sample, as mentioned earlier.

4. Results and Analyses

We used Equation (8) to model the *M*–*R* relationship of the iron-rock and ice-gas planets of Tables 1 and 2. The parameter $c_0 (= \frac{4}{3}\pi\rho_D)$ and the fractal dimension D were obtained by optimization using the ordinary least squares (OLS) method in the $\log_{10}(M) \times \log_{10}(R)$ relation. The coefficient of determination R-squared and the correlation coefficient R are $\simeq$0.9 for both fits of Equation (8) for the *M*–*R* relationship of the iron-

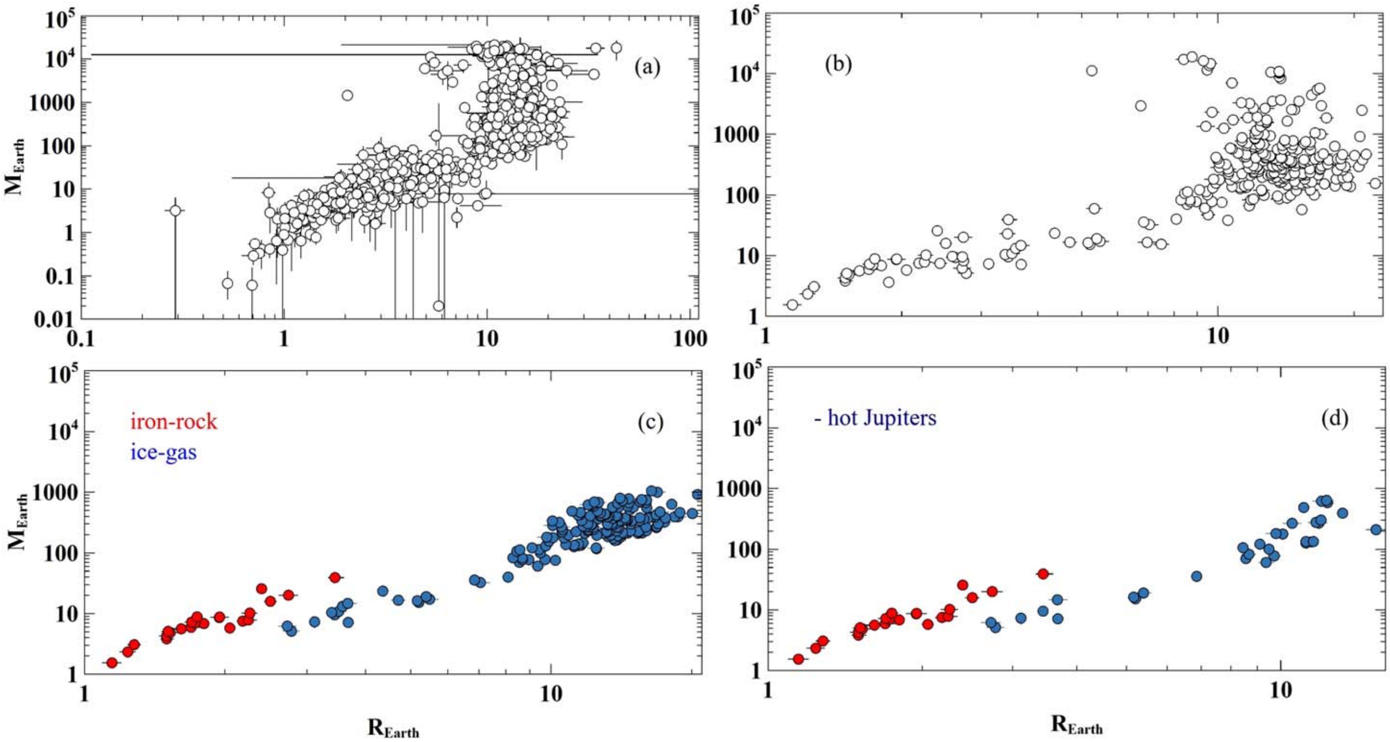

Figure 2. The filtering process for planetary bodies in the raw data. (a) Original sample. (b) Constraint in the relative uncertainties DM < 14.3% and DR < 4.8%. (c) Exclusion of objects with mass >1300 $M_{\oplus}$ (or $\simeq$4 M_J) and constraining the likely internal composition of the planet. (d) Excluding possible hot Jupiters from the sample of ice-gas planets.

rock and ice-gas planets (Figure 3). This means that almost 90% of the variability of M is explained by R and that there is a very strong direct relationship between these two variables. The OLS model assumes normality for the residual errors. The Shapiro–Wilk test yields a p-value of 0.06 and 0.206 for the distribution of the residuals of the fits for ice-gas and iron-rock planets, respectively. The residual errors are assumed to be normally distributed, with a confidence level of $\alpha = 0.05$. The data contain no outliers when considering the range of $\pm 3\sigma$ in the residual errors. The relative uncertainties of the parameters c_0 and D are smaller than 8%.

The observed masses of some planets in the solar system differ from the theoretical values obtained from Equation (8) when using the parameters D and c_0 from Figure 3. The largest discrepancies between the model and observed masses are 164% and 118% for Mars and Mercury, respectively. These differences can be explained by the nature of the data; 72% of the ice-gas planets have densities less than 1.0 g cm^{-3} and 96% of the iron-rock planets have densities greater than 5.3 g cm^{-3} (Figure 4(a) and (b)). These density ranges are well distributed across the planetary radius for both samples (Figure 4(c)). Mars and Mercury have densities of 3.9 and 5.4 g cm^{-3}, respectively, which are outside or nearly outside the density range of most planets in the sample, justifying their larger discrepancies. Nevertheless, the fractal M–R relation estimated from our sample of iron-rock and ice-gas planets has reasonable predictive power for super-Earths and hot Saturns, such as TOI-1452 b and HAT-P-17 b respectively, and even for solar system icy moons such as Ganymede (Jupiter III) and Titan (Saturn VI). These objects have radii of 1.67 ± 0.07, 11.3 ± 0.3, 0.413 and 0.404 $R_{\oplus}$, resulting in predicted masses of 5.5, 188, 2.48×10^{-2} and 2.34×10^{-2} $M_{\oplus}$ respectively. These predicted masses yield discrepancies of 15.4%, 10.7%, 0.8% and 3.8% relative to the masses of 4.8 ± 1.3, (Cadieux et al. 2022) 170 ± 6 (Howard et al. 2012), 2.50×10^{-2} (Showman & Malhotra 1999) and 2.25×10^{-2} $M_{\oplus}$ (Jacobson et al. 2006), respectively.

The fractal dimension D is nearly identical for ice-gas and iron-rock planets, suggesting that these objects are likely to have a similar degree of heterogeneity in their density and a similar or very similar composition in each sample. $D < 3$ is not a consequence of the cut-off applied in the samples of Tables 1 and 2. For example, if we exclude the precision constraint and keep the cut-offs for planet mass and density, we obtain $D = 2.6$ for ice-gas planets (483 objects) and $D = 2.8$ for iron-rock planets (216 objects) in the D error bars defined in Figure 3, but with a loss of predictive power due to the larger dispersion of mass at the same radius. The discrepancy in the

Table 1
Sample of Iron-rock Planets Sorted by Increasing Mass

Planet	M	R	[Fe/H]	SP
LTT 1445A c	1.5 ± 0.2	1.15 ± 0.05	−0.34	M
LHS 1478 b	2.3 ± 0.2	1.24 ± 0.05	−0.13	M3.5 V
TOI-431 b	3.1 ± 0.3	1.28 ± 0.04	0.2	
Kepler-36 b	3.8 ± 0.1	1.50 ± 0.04	−0.18	
HD 219134 b	4.3 ± 0.3	1.50 ± 0.06	0.11	K3 V
GJ 9827 b	4.9 ± 0.4	1.53 ± 0.06	−0.28	K6 V
K2-141 b	5.1 ± 0.4	1.51 ± 0.05	−0.0	
HD 80653 b	5.6 ± 0.4	1.61 ± 0.07	0.28	G2
K2-146 b	5.77 ± 0.08	2.05 ± 0.06	−0.02	M3.0 V
TOI-1235 b	5.9 ± 0.6	1.69 ± 0.08	0.33	M0.5 V
WASP-47 e	6.8 ± 0.7	1.80 ± 0.02	0.38	G9 V
LHS 1140 b	7.0 ± 0.9	1.73 ± 0.03	−0.24	M4.5
TOI-402 b	7.2 ± 0.8	1.70 ± 0.06	0.03	
K2-146 c	7.5 ± 0.1	2.2 ± 0.07	−0.02	M3.0 V
HD 97658 b	$7.8^{+0.5}_{-0.4}$	$2.3^{+0.1}_{-0.09}$	−0.23	K1 V
55 Cnc e	8.6 ± 0.4	1.95 ± 0.04	0.31	K0 IV-V
HD 213885 b	8.8 ± 0.7	1.74 ± 0.05	−0.04	G
K2-314 b	9 ± 1	1.95 ± 0.09	0.2	G8 IV/V
TOI-1062 b	$10.2^{+0.9}_{-0.8}$	$2.26^{+0.09}_{-0.08}$	0.14	
HD 207897 b	16 ± 2	2.50 ± 0.08	−0.04	K0
HIP 97166 b	20 ± 1	2.7 ± 0.1	0.27	
Kepler-411 b	26 ± 3	2.40 ± 0.06	0.23	K2 V
TOI-849 b	39 ± 3	$3.4^{+0.2}_{-0.1}$	0.19	G

Note. M and R are the mass and radius of the planet with respect to the mass and radius of the Earth respectively. [Fe/H] and SP are the metallicities and spectral types of the planet's parent star respectively.

Table 2
Sample of Ice-gas Planets

Planet	M	R	[Fe/H]	SP
Kepler-26 b	$5.1^{+0.7}_{-0.6}$	2.8 ± 0.1	−0.13	M0 V
Kepler-26 c	6.2 ± 0.7	2.7 ± 0.1	−0.13	M0 V
Kepler-36 c	7.1 ± 0.2	$3.67^{+0.10}_{-0.09}$	−0.18	
Kepler-11 d	7^{+2}_{-1}	$3.11^{+0.07}_{-0.06}$	0	G
KOI-142 b	10 ± 1	3.44 ± 0.08	0.27	G6 V
K2-314 c	15 ± 2	$3.7^{+0.2}_{-0.1}$	0.2	G8 1V/V
Kepler-25 c	15^{+2}_{-1}	5.21 ± 0.07	−0.04	
TOI-421 b	16 ± 1	5.2 ± 0.1		
K2-24 b	19 ± 2	5.4 ± 0.2	0.34	G9 V
HD 89345 b	36 ± 3	6.9 ± 0.1	0.45	G
HD 221416 b	61 ± 6	9.4 ± 0.3	−0.08	K0 IV/V
Kepler-34 (AB) b	70 ± 3	8.6 ± 0.2	−0.	
HD 332231 b	78 ± 7	9.7 ± 0.3	0.036	F8
EPIC 246193072 b	83 ± 7	8.7 ± 0.3	0.098	
K2-287 b	100 ± 9	9.5 ± 0.1	0.20	
Kepler-16 (AB) b	106 ± 5	8.44 ± 0.03	−0.3	K
K2-139 b	121 ± 14	9.1 ± 0.2	0.24	K0 V
K2-232 b	126 ± 12	11.2 ± 0.2	0.1	F9 V
HD 1397 b	132 ± 6	11.5 ± 0.3	0.27	G5 III
TOI-201 b	133 ± 10	11.2 ± 0.2	0.24	F6 V
Kepler-289 c	133 ± 16	11.6 ± 0.2	0.05	
TOI-216 c	178 ± 6	10.1 ± 0.2	−0.15	
Kepler-56 c	181^{+21}_{-19}	9.8 ± 0.5	0.2	
TOI-1899 b	210 ± 22	15.3 ± 0.7	0.31	M0
CoRoT-9 b	267 ± 22	10.5 ± 0.4	−0.01	G3 V
TOI-1478 b	269^{+17}_{-15}	11.9 ± 0.4	0.08	
K2-99 b	276 ± 6	11.7 ± 0.4	0.21	G0 IV
TOI-892 b	302 ± 22	12.0 ± 0.2		
TOI-677 b	393 ± 22	13.2 ± 0.3	0.00	
TOI-481 b	486 ± 10	11.1 ± 0.1		
Kepler-117 c	585 ± 57	12.3 ± 0.4	−0.04	F8 V
HAT-P-15 b	618 ± 21	12.0 ± 0.5	0.22	G5
Kepler-30 c	639 ± 51	12.3 ± 0.4	0.18	

mass of HAT-P-17 b changes from 10.7% to 64.2% with this new data fit. Similarly, if we include the hot Jupiters (158 objects) and consider the precision and mass constraints, we obtain $D = 2.9$, which means that objects with approximately the same density are more important in the new fit.

The degree of heterogeneity of the planets in our sample is lower than that in the solar system. The fractal dimension D and constant c_0 of the solar system planets are 2.40 ± 0.01 and 0.59 ± 0.01, respectively. These values are a consequence of their density range ($0.7 \leqslant \rho \leqslant 5.5$ g cm^{-3}), which overlaps with the density range of ice-gas and iron-rock planets, suggesting planets with different compositions. Not surprisingly, fitting the solar system M–R data with Equation (8) yields an R-squared coefficient of 0.99, well above the value obtained with our samples. This result can be justified by the high accuracy of the mass and radius determined *in loco* for all planets in the solar system. If we divide the solar system into terrestrial and gas giant planets, we get $D = 3.2$ and 2.4, respectively. It is obvious that the value for terrestrial planets is unrealistic because the internal gravitational force is compensated by the strength of the material it is made of. The actual value is a consequence of the presence of Mars in the sample, which makes the fit of the M–R power law steeper in a log–log plot. Without Mars, $D \simeq 3.0$, which is reasonable because of the smaller variations in density of Earth, Venus and Mercury (5.2–5.5 g cm^{-3}). The dimension $D = 2.4$ obtained from the ice and gas giants expresses the heterogeneity of the density of the sample (between 0.7 g cm^{-3} of Saturn and 1.6 g cm^{-3} of Neptune). The heterogeneity of the density of the gas giants is larger than that observed in the sample of terrestrial planets.

The ratio of fractal densities of rocky and gaseous planets is about five, which is reflected in the scale difference ("gap") between these two populations in Figure 3. This gap likely reflects the original distinction between these two populations based on location in the protoplanetary disk, atmospheric opacity, and minimum core mass of the planetary embryo, as previously suggested by Piso & Youdin (2014) and Lambrechts & Lega (2017). The gap reduces the fractal exponent D of Equation (8) obtained from a combined sample of iron-rock and ice-gas planets. This phenomenon is observed in the solar system and its existence was suggested by Figure 1. There are several examples of this selection effect in the literature: the

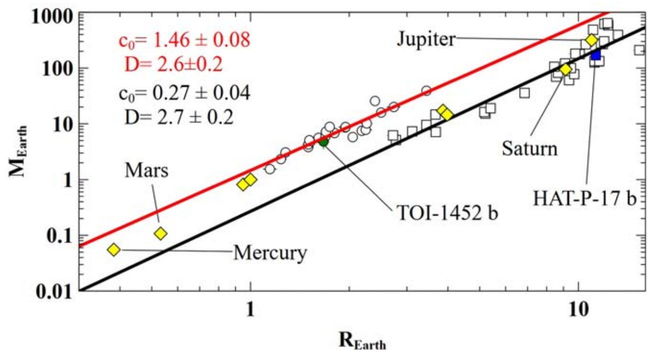

Figure 3. $M \times R$ relation for iron-rock (circles) and ice-gas (squares) planets. The red and black lines show the fit of Equation (8) in these two samples. The solar system planets, the super-Earth TOI-1452 b and hot Saturn HAT-P-17 b are yellow diamonds, green circles and blue squares, respectively, not included in the fit. Solar system data are from Cox (2000).

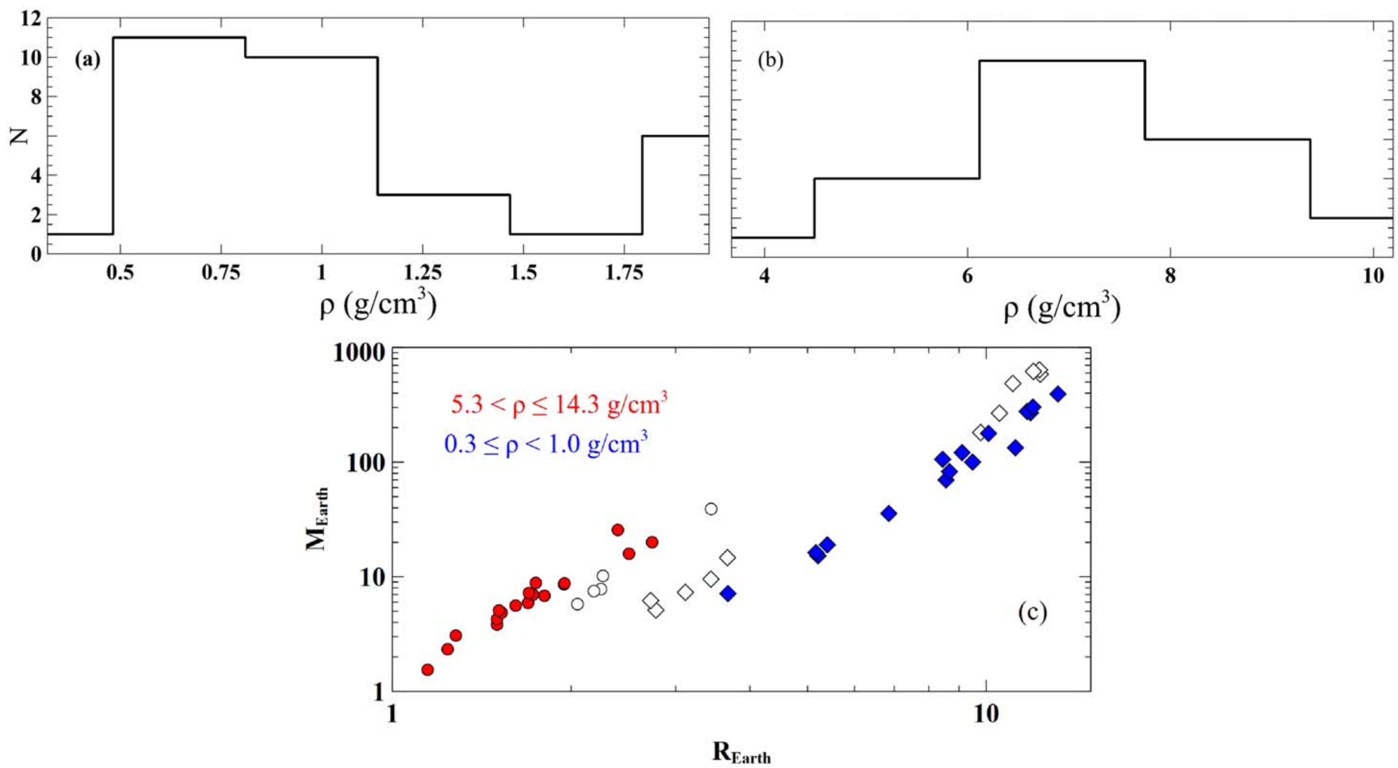

Figure 4. Histograms of the density of ice-gas (a) and iron-rock (b) planets. (c) Distribution of density along the M–R relation of ice-gas (diamonds) and iron-rock (circles) planets.

exponents D calculated from a combined sample of Tables 1 and 2 are 1.5 ± 0.1 and 1.7 ± 0.3 using a mass threshold of >25 and <124 $M_{\oplus}$ from Bashi et al. (2017) and Otegi et al. (2020) (Figure 5(a)). The D values derived from these latter works are 1.82 ± 0.07 and 1.6 ± 0.1, similar to our coefficients.

The relationship between dimension D and index n is $D = 3 - n/1 - n$, which is obtained by comparing Equations (2) and (8). The weighted average dimension D is 2.6 ± 0.1, implying $n = -0.25 \pm 0.04$. Polytropes with $n < 1$ can describe some models of interstellar clouds (e.g., Shu et al. 1972). Viala & Horedt (1974) argue that for these polytropes, as the radius increases, the density increases for $-1 < n < 0$ and the temperature decreases for $-1 < n < \infty$. These conditions are not observed and do not even apply to planets. It is more reasonable to assume that the objects in our sample have approximately constant density and suffer little compression from the overlying material. Presumably, the fractal dimension $D \rightarrow 3$ for a narrow density range $\Delta\rho \rightarrow 0$. In fact, the fractal

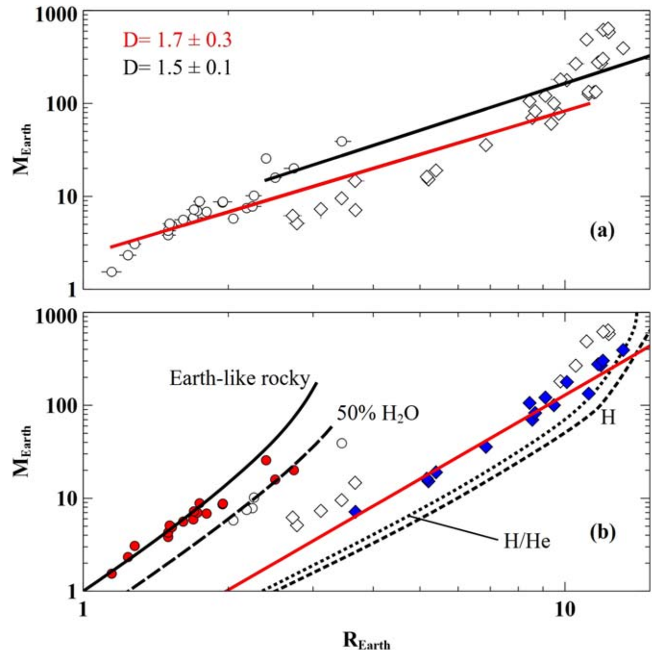

Figure 5. (a) Fractal dimensions D estimated with mass threshold of <124 and >25 $M_\oplus$ from Bashi et al. (2017) (red line) and Otegi et al. (2020) (black line). (b) M–R relations derived from EoS for different planet compositions superimposed on the sample of ice-gas planets (diamonds) and iron-rock planets (circles): hydrogen (H) and helium (He) mixture with 25% helium by mass (H/He) from Seager et al. (2007); Earth-like Rocky (32.5% Fe+67.5% $MgSiO_3$) and 50% H_2O (50% Earth-like rocky core + 50% H_2O layer by mass), assuming a surface pressure of 1 millibar and a temperature of 300 K from Zeng et al. (2019). Red corresponds to planets with density in the range of $5.3 < \rho \leqslant 14.3$ and blue in the range of $0.3 \leqslant \rho < 1.0$ g cm^{-3}. The red solid line corresponds to $M = (0.129 \pm 0.002)R^3$ for ice-gas planets in the density range of $0.3 \leqslant \rho < 1.0$ g cm^{-3}.

dimensions are $D = 2.87 \pm 0.05$ ($n = -0.07 \pm 0.02$) for iron-rock planets and 3.18 ± 0.04 ($n = 0.08 \pm 0.01$) for ice-gas planets with $5.3 < \rho \leqslant 14.3$ g cm^{-3} and $0.3 \leqslant \rho < 1.0$ g cm^{-3}, respectively. Most of the planets in our sample lie in these narrower density ranges (see Figure 4). The relative error in fitting Equation (8) to the M–R relationship of the planets of Tables 1 and 2 is only 8%. This discrepancy is related to the compositional and density scatter of the planets (see Figure 5(b)) rather than to a systematic error in the M–R ratio of some planets from these tables. As shown, this relative error becomes 2% for the ice-gas planets in a narrower density range.

The median discrepancy between the masses of ice-gas planets with radii >10 $R_\oplus$ and about 100 $M_\oplus$ compared to expectations from the relation $M \propto R^3$ is 25%, twice as much as the rest of this sample (Figure 5(b)). Ice-gas planets with radii larger than 10 $R_\oplus$ show a possible variation in their internal composition compared to the rest of the sample, as the H/He fraction increases from a planet with similar mass to Neptune to Saturn (Zeng et al. 2019), and the increasing importance of electron degeneracy pressure at $M > M_J$. The mass variation of these planets with radii >10 $R_\oplus$ increases D above 3, but this sample has a high dispersion in mass for an almost equal radius and a presence of outliers, like Mars in our terrestrial planet sample, could not be excluded. This compositional and physical variation with planetary radius could explain the R coefficient of the fits to Equation (8) and the unrealistic negative polytropic index. In fact, $D = 2.86 \pm 0.05$ for ice-gas planets with $0.3 \leqslant \rho < 1.0$ g cm^{-3} when distinguishing planets with radii >10 $R_\oplus$ from the fit of Equation (8).

Based on our previous results, we empirically propose an upper mass limit of about 100 $M_\oplus$ for ice-gas planets described by $R \propto M^{1/3}$, since $n \to 0$, $D \to 3$ for a narrow density range. This value is above the limits of 30 and below 318 $M_\oplus$ (or 1 M_J) presented in Section 2. However, this mass threshold may change depending on the constant density of the planetary sample under consideration. A family of power laws $M \sim R^3$ could be found in an exoplanet sample. These power laws are parallel to each other in a log–log M–R diagram and the scaling factor for their differentiation is the constant c_0, which is proportional to the density ($\rho_D = \rho$).

5. Summary

We investigated the M–R relation of a selected sample of ice-gas and iron-rock exoplanets using a fractal approach to their densities. Our main results are:

1. The average fractal dimension $D = 2.6 \pm 0.1$ determined from the M–R relation of a sample of ice-gas and iron-rock planets indicates that these objects are likely to have a similar degree of heterogeneity in their densities and a nearly similar composition in each sample.

2. A scale difference generates a "gap" between ice-gas and iron-rock planets. This gap is a direct consequence of the density range of these samples. This scale difference can reduce the fractal exponent D of Equation (8) of a combined sample of iron-rock and ice-gas planets, increasing the degree of heterogeneity of the sample.
3. The M–R relations based on our sample are $M = (1.46 \pm 0.08)R^{2.6\pm0.2}$ for the rocky population ($3.6 \leqslant \rho \leqslant 14.3$ g cm^{-3}), with $1.5 \leqslant M \leqslant 39$ $M_\oplus$, and $M = (0.27 \pm 0.04)R^{2.7\pm0.2}$ for ice-gas planets ($0.3 \leqslant \rho \leqslant 2.1$ g cm^{-3}) with $5.1 \leqslant M \leqslant 639$ $M_\oplus$ (or $\simeq 2M_J$) and orbital periods greater than 10 days.
4. We empirically propose an upper mass limit of about 100 $M_\oplus$ for ice-gas planets described by $R \propto M^{1/3}$, since $n \to 0$ and $D \to 3$ for a narrow density range $\Delta\rho \to 0$. However, this mass threshold may change depending on the constant density of the considered planetary sample.

Acknowledgments

The authors thank Orahcio Felicio de Sousa for his comments and suggestions during the preparation of this manuscript and an anonymous reviewer for constructive comments and recommendations that definitely helped to improve the readability and quality of the article.

References

Armstrong, D. J., Lopez, T. A., Adibekyan, V., et al. 2020, Natur, 583, 39
Bashi, D., Helled, R., Zucker, S., & Mordasini, C. 2017, A&A, 604, A83
Baumeister, P., MacKenzie, J., Tosi, N., & Godolt, M. 2018, in European Planetary Science Congress, EPSC2018–678
Bruderer, S., van der Marel, N., van Dishoeck, E. F., & van Kempen, T. A. 2014, A&A, 562, A26
Cadieux, C., Doyon, R., Plotnykov, M., et al. 2022, AJ, 164, 96
Carpinteri, A., & Ferro, G. 1994, Materials and Structures, 27, 563
Chen, G., & Cheng, Q. 2017, JGRB, 122, 1919
Cheng, Q. 2017, in First Complex Systems Digital Campus World E-Conf., ed. P. Bourgine, P. Collet, & P. Parrend (Cham: Springer), 395
Cox, A. N. 2000, Allen's Astrophysical Quantities (New York: Springer)
Dawson, R. I., & Johnson, J. A. 2018, ARA&A, 56, 175
de La Fuente Marcos, R., & de La Fuente Marcos, C. 2006, A&A, 452, 163
Drake, A. J., & Cook, K. H. 2004, ApJ, 604, 379
Dressing, C. D., & Charbonneau, D. 2015, ApJ, 807, 45
Duck, A., Gaudi, B. S., Eastman, J. D., & Rodriguez, J. E. 2022, An Exploration of Systematic Errors in Transiting Planets and their Host Stars, arXiv:2209.09266
Endl, M., Cochran, W. D., Tull, R. G., & MacQueen, P. J. 2003, AJ, 126, 3099
Guillot, T. 1999, Sci, 296, 72
Hatzes, A. P., & Rauer, H. 2015, ApJL, 810, L25
Howard, A. W., Bakos, G. Á, Hartman, J., et al. 2012, ApJ, 749, 134
Jackson, I. 1998, GeoJI, 134, 291
Jacobson, R. A., Antreasian, P. G., Bordi, J. J., et al. 2006, AJ, 132, 2520
Katyal, N., Banerjee, V., & Puri, S. 2014, JQSRT, 146, 290
Lambrechts, M., & Lega, E. 2017, A&A, 606, A146
Landais, F., Schmidt, F., & Lovejoy, S. 2019, Icar, 319, 14
Li, Y.-P. 2020, in Origins: From the Protosun to the First Steps of Life Vol. 345, ed. B. G. Elmegreen, L. V. Tóth, & M. Güdel, 355
Lissauer, J. J., Dawson, R. I., & Tremaine, S. 2014, Natur, 513, 336
Mandelbrot, B. B. 1982, The Fractal Geometry of Nature, Vol. 1 (New York: W. H. Freeman)
Miranda, J. G., Montero, E., Alves, M., Paz-González, A., & Vázquez, E. 2006, Geode, 134, 373
Mulders, G. D. 2018, in Handbook of Exoplanets, ed. H. J. Deeg & J. A. Belmonte, 153
Odrzywolek, A., & Rafelski, J. 2018, AcPPB, 49, 1917
Otegi, J. F., Bouchy, F., & Helled, R. 2020, A&A, 634, A43
Owen, J. E., & Kollmeier, J. A. 2017, MNRAS, 467, 3379
Pardo-Igúzquiza, E., & Dowd, P. A. 2022, Icar, 384, 115109
Paz-González, A., Miranda, J. G., & Vazquez, E. 2010, Vadose Zone J., 9, 3259
Peak, D. 1992, ASNYN, 4, 7
Piso, A.-M. A., & Youdin, A. N. 2014, ApJ, 786, 21
Queloz, D., Cassen, P., Udry, S., et al. 2007, Extrasolar Planets: Saas Fee Advanced Course 31 (Berlin: Springer)
Seager, S., Kuchner, M., Hier-Majumder, C. A., & Militzer, B. 2007, ApJ, 669, 1279
Showman, A. P., & Malhotra, R. 1999, Sci, 296, 77
Shu, F. H., Milione, V., Gebel, W., et al. 1972, ApJ, 173, 557
Siekman, W. H. 2001, JPhA, 34, 1949
Sotin, C., Grasset, O., & Mocquet, A. 2007, Icar, 191, 337
Teles, S., Lopes, A. R., & Ribeiro, M. B. 2021, PhLB, 813, 136034
Thorngren, D. P., Fortney, J. J., Murray-Clay, R. A., & Lopez, E. D. 2016, ApJ, 831, 64
Tucker, E., & Nepsky, P. 2011, Polytropic Planets
Vázquez, E., Miranda, J. G., & Paz-González, A. 2005, Ecological Modelling, 182, 337
Viala, Y. P., & Horedt, G. 1974, A&A, 33, 195
Vinet, P., Ferrante, J., Smith, J. R., & Rose, J. H. 1986, Temperature Effects on the Universal Equation of State of Solids
Wagner, F. W., Tosi, N., Sohl, F., Rauer, H., & Spohn, T. 2012, A&A, 541, A103
Zeng, L., Jacobsen, S. B., Sasselov, D. D., et al. 2019, PNAS, 116, 9723